

# Scaling relation for occulter manufacturing errors

Dan Sirbu<sup>1,4</sup>, Stuart B. Shaklan<sup>2</sup>, N. Jeremy Kasdin<sup>1</sup>, Robert J. Vanderbei<sup>3</sup>

<sup>1</sup> Department of Mechanical and Aerospace Engineering, Princeton University

<sup>2</sup> NASA Jet Propulsion Laboratory, 4800 Oak Grove Drive, Pasadena, CA

<sup>3</sup> Department of Operations Research and Financial Engineering, Princeton University

<sup>4</sup> NASA Ames Research Center, Moffett Field, Mountain View, CA

## ABSTRACT

An external occulter is a spacecraft flown along the line-of-sight of a space telescope to suppress starlight and enable high-contrast direct imaging of exoplanets. The shape of an external occulter must be specially designed to optimally suppress starlight; however, deviations from the ideal shape such as manufacturing errors can result in loss of suppression in the shadow. Due to the long separation distances and large dimensions involved for a space occulter, laboratory testing is conducted with scaled versions of occulters etched on silicon wafers. Using numerical simulations for a flight Fresnel occulter design, we show how the suppression performance of an occulter mask scales with the available propagation distance for expected random manufacturing defects along the edge of the occulter petal. We derive an analytical model for predicting performance due to such manufacturing defects across the petal edges of an occulter mask and compare this with the numerical simulations. We discuss the scaling of an extended occulter testbed.

**Keywords:** External Occulters, Starshades, High Contrast Imaging, Scaling, Scalar Diffraction, Optical Verification

## 1. INTRODUCTION

With over 4,000 exoplanet candidates and over 1,000 confirmed exo-planets discovered using principally indirect detection methods, direct imaging allows for characterization and spectral measurements of their reflected light and is of great interest as the next major step in exoplanet science. Direct imaging for an Earth-like planet is a challenging task because of the ten orders of magnitude contrast ratio between the bright star and its dim rocky planetary companion and due to the small angular separation that covers the habitable zone.

An external *occulter*, also called a starshade, is a mission concept that involves a specially-shaped spacecraft flying in formation with the space telescope. The occulter is placed along the line-of-sight of the telescope and target star and suppresses most of the stellar flux before it reaches the telescope pupil allowing for the high-contrast imaging of exoplanets. The edge of the occulter has to be designed to minimize diffraction and create a shadow over a region that will cover the telescope's diameter and an additional alignment margin for the formation flight. Optimization methods can be used to suppress starlight to the necessary factor of  $10^{-10}$  contrast for imaging an exo-Earth, with the size of the occulter, observation wavelengths, and manufacturing limitations incorporated as optimization constraints. Proposed designs range from flagship-class such as THEIA<sup>1</sup> to smaller missions such as the recent EXO-S mission design.<sup>2</sup>

Experimental verification of occulter designs is an important part of the technological development for an occulter mission. Full-scale petals have been built and assembled; their individual edge shape and assembled configuration has been precisely and repeatedly measured to predict the optical performance based on existing manufacturing capabilities.<sup>3</sup> Nevertheless, the performance prediction is based on the same scalar diffraction models used to design the occulter shape. Because a full-scale occulter cannot be tested on the ground, it is therefore important to experimentally verify the performance of scaled occulters in the laboratory to validate the scalar diffraction optical models used for their design and performance prediction. These scaled occulter designs are etched onto silicon wafers. However, the etching process introduces deviations from the ideal specified shape (we refer to these as manufacturing errors throughout this paper).

Table 1: Summary of operational Fresnel numbers for different occulter designs comparing the Existing Princeton Occulter Experiment (EPOE) with the Proposed Princeton Occulter Experiment (PPOE) and two reference mission designs (THEIA and O3).

Design	Occulter Radius, $R$	Separation, $z$	Wavelength, $\lambda$	Fresnel Number
THEIA	20 m	55,000 km	600 nm	12.1
O3	17 m	19,500 km	600 nm	24.7
EPOE	188 m	97,000 km	600 nm	607
PPOE	21.9 m	55,000 km	600 nm	14.5

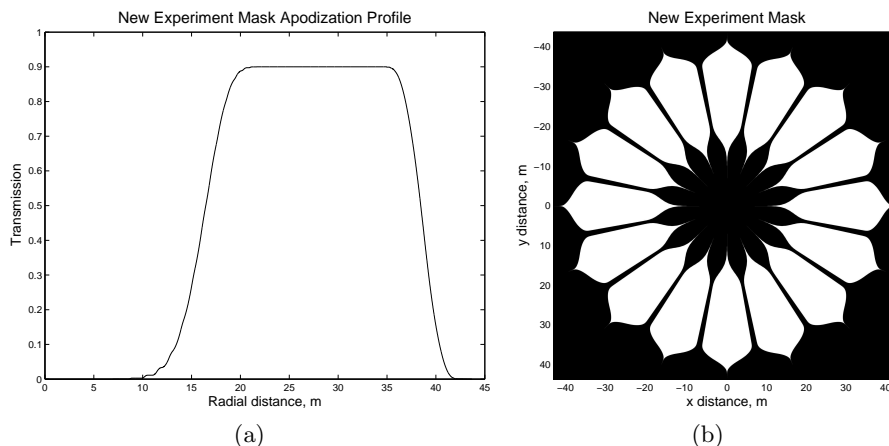


Figure 1: (a) Designed apodization profile including outer ring and struts (b) Binary realization of mask profile.

The main contribution of this paper is to quantify the effect on suppression of the random edge deviations introduced by the manufacturing process for a mask scaled at different propagation distances. This is necessary to allow the design of the new Proposed Princeton Occulter Experiment (PPOE) which will be a testbed with a longer propagation distance compared to the Existing Princeton Occulter Experiment (EPOE). The study in this paper allows us to choose an operating scale of the PPOE in terms of the relation of the expected manufacturing errors to the mask size to measure near ideal suppression levels. More specifically, in this paper we:

- Review the occulter scaling process, compare the dimensions of the PPOE with the EPOE, and present the baseline occulter mask used to evaluate the performance of the PPOE (**Section §2**).
- Summarize the two-dimensional numerical diffraction model that we previously developed and verified against experimental results in the EPOE<sup>4</sup> (**Section §3**).
- Present simulation results of suppression performance as a function of occulter manufacturing deviation for the PPOE. We also rescale the testbed at different propagation distances and compare corresponding suppression performance (**Section §4**).
- Develop an analytical power law model for performance due to edge defects and compare this to simulation results from the numerical model (**Section §5**).
- Summarize the selected PPOE dimensions and the expected suppression performance levels (**Section §6**).

## 2. OCCULTER DESIGN AND SCALING

Optimization methods can be used to design an occulter apodization profile that creates a dark shadow downstream from the occulter,<sup>5</sup> which can then be turned into a binary occulter profile by petalization.<sup>6</sup> The linear programming optimization process used is described in more detail in previous papers.<sup>7-9</sup>

Table 2: Summary of final scaled occulter parameters for a testbed with a 76 m total propagation distance available and a design reference of 100 m total propagation distance.

Parameter	Space Design	Collimated Scale		Diverging Scale	
Separation distance, $z$	55,000 km	38 m	50 m	38 m	50 m
Distance scale, $a$	1	1200	1050	1200	1050
Source distance, $h$	$\infty$	$\infty$	$\infty$	38 m	50 m
Divergence scale, $\gamma$	1	1	1	1.4	1.4
Inner radius, $R_{\text{inn}}$	21.9 m	18.2 mm	20.8 mm	12.8 mm	14.7 mm
Outer radius, $R_{\text{out}}$	43.7 m	36.4 mm	41.7 mm	25.8 mm	29.4 mm
Dark shadow radius, $\rho_{\text{dark}}$	2.6 m	2.2 mm	2.5 mm	3.1 mm	3.5 mm
Outer shadow radius, $\rho_{\text{out}}$	43.7 m	36.4 mm	41.7 mm	51.5 mm	57.8 mm
Telescope diameter, $D$	4 m	3.3 mm	3.8 mm	3.3 mm	3.8 mm

In the EPOE, the occulter mask is oversized compared to a realistic design that would be flown in space. The rationale to oversize the design arose due to the limited propagation distance available in the occulter testbed – an oversized design means that when scaled to laboratory size the occulter can fill the silicon wafer, and fixed manufacturing errors on the  $\mu\text{m}$  level represent a smaller percentage of that mask. Here, we explore scaling of a realistic occulter design for a testbed with a longer propagation distance so that a realistic space design can be experimentally tested. In Table 1 we compare the Fresnel number ( $\frac{R^2}{\lambda z}$ ) for the inner occulter mask used in the EPOE and PPOE occulter designs with two design reference missions at 600 nm: THEIA<sup>1</sup> is a flagship-class mission designed for a 4-m telescope, and O3<sup>10</sup> is a probe-class mission designed for a smaller 1.1 m telescope.

The EPOE laboratory mask design uses an outer ring to minimize diffraction from the finite size of the input beam and laboratory dimensions, a set of support struts that can be shown to theoretically not introduce diffractive structure across the optimized dark hole portion of the shadow. Additionally, the mask is used with an expanding beam to mitigate surface feature effects of any optics upstream from the occulter. The occulter is designed for a plane input wave at space dimensions. Two scalings are subsequently applied:<sup>9</sup> first a scaling to laboratory separation, and second a scaling to account for the expanding input beam.

For the PPOE mask design we have maintained all the design features outlined above for EPOE, but are using an inner occulter operating at a realistic space Fresnel number. In Figure 1 we show the occulter design we use throughout this paper. Figure 1(a) shows the combined transmission profile for an optimized inner occulter with an optimized outer ring and supporting struts. The optimization of this particular design is described in more detail elsewhere.<sup>11</sup> The corresponding binary mask realization with 16-petals is shown in Figure 1(b). Both the apodization profile and the binary mask are shown at designed space dimensions.

The PPOE is a new testbed predicated on extending the total propagation distance compared to the original 10 m available for the EPOE. We have investigated total propagation distances available for PPOE in the range of 10 m to 140 m. We use a 100 m total propagation distance as a baseline for simulations. Based on the simulation results in Section 4, a final selected testbed location was chosen with a 76 m total propagation distance available; the scaling of the PPOE parameters from space design to both the actual 76 m and the 100 m baseline are summarized in Table 2. Additionally, the diameter of the occulter mask is maximized for the diverging scaling corresponding to  $h = z$ ; the occulter mask is placed halfway between the artificial diverging point source and the telescope location.

### 3. NUMERICAL MODEL

The oversized nature of EPOE allows spatially resolving the source of scattered light, and thus it is easier to disambiguate the sources of error. We have developed an optical propagation approach that modeled edge defects, and previously employed this model to compare against laboratory performance measurements of the EPOE.<sup>4</sup> This propagation model uses two-dimensional Fresnel propagation via Matrix Fourier Transforms.<sup>12</sup> Thus, we can directly model almost any type of non-idealization including edge manufacturing defects. This approach is fairly

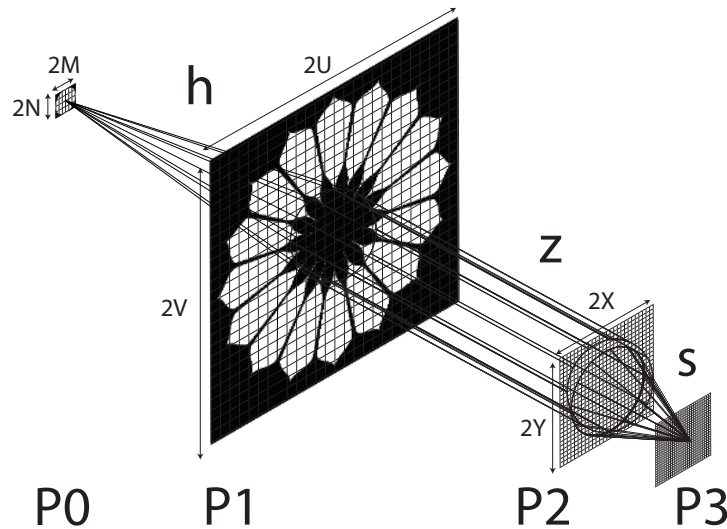


Figure 2: Optical propagation planes for two-dimensional diffraction model.

computationally expensive, and to make this approach numerically tractable we introduce anti-aliasing at the edges of the occulter mask in order to represent a higher-resolution mask.

The same model can be used to model diffraction effects in the PPOE. We refer to Figure 2 to describe the propagations between the different planes involved in the occulter testbed. We define four planes of propagation: P0 is the plane of the pinhole source ( $2M \times 2N$  in physical size), P1 is the plane of the occulter mask ( $2U \times 2V$  in physical size), P2 is the pupil plane where the telescope aperture lies and where we measure the *suppression* of the shadow ( $2X \times 2Y$  in physical size), and lastly P3 is the focal plane of the telescope and the plane in which we measure the *contrast* of the point spread function. Thus, to obtain the point spread function (PSF) of the occulter testbed we need three separate Fresnel propagations across distances  $h$ ,  $z$ , and  $s$  respectively between these four planes.

We use a two-dimensional mask model across P1. The mask model has  $n \times n$  samples, and it is allowed to take on gray values at the petal edges. The gray value is computed by  $g \times g$  anti-aliasing. Therefore, a mask model with  $(n, g)$  and with radius  $R$  will therefore be representative of the resulting feature size given by  $\delta R = 2R/n/g$ .

To simulate manufacturing defects, we isolate all the gray pixels along a petal contour and add or subtract to the gray area the corresponding area of a set of circular defects with varying diameters. A set of circular defect diameters representing the edge perturbation along one petal is generated as white noise with a specified root-mean-squared (RMS) level.

#### 4. SIMULATION RESULTS

The ideal performance of the occulter mask assuming a perfect realization using sixteen petals can be computed using the Jacobi-Anger expansion of the one-dimensional Fresnel propagation of the occulter mask's transmission profile following the same procedure as described in previous work.<sup>4</sup> The effect of finite feature sizes can be computed using the two-dimensional mask model without introducing any circular defects along the edges. In Table 3, we have listed several numerical mask models of the PPOE design with their feature sizes listed both at a scaled 100 m total propagation distance and at space scale. Using the two dimensional Fresnel propagation equations, we compute the suppression at the pupil plane across the telescope aperture and the corresponding contrast in the annular working region for the different manufacturing feature accuracies. For comparison, the first experimental results obtained in the EPOE were limited by edge features and manufacturing defects on the order of  $5\mu\text{m}$ . Currently, a typical occulter shape etched on silicon can maintain  $0.5\mu\text{m}$  feature accuracy,

Table 3: Suppression and contrast performance for different manufacturing feature accuracies corresponding to the PPOE mask design scaled at a 100 m total propagation distance for a monochromatic diverging input beam at 633 nm.

Lab Feature Size $\delta R, \mu\text{m}$	Mask Model $n \times n$	Model $g \times g$	Space Scale Feature mm	Suppression $\text{Log}_{10}$	Contrast $\text{Log}_{10}$
9.8	6,000	1	16.7	-5.36	-8.04
7.4	4,000	2	12.5	-5.52	-8.44
4.9	6,000	2	8.3	-5.89	-9.06
2.0	6,000	5	3.3	-6.97	-9.83
1.4	6,000	7	2.4	-7.90	-10.4
1.0	6,000	10	1.7	-8.44	-10.8
0.5	12,000	10	0.8	-9.27	-11.2
0.3	6,000	40	0.4	-9.49	-11.3
0.1	6,000	100	0.2	-9.77	-11.4
Ideal	N/A	N/A	Ideal	-9.82	-11.4

and improvements in the manufacturing process are expected to generate an improved feature accuracy of 0.2  $\mu\text{m}$ .<sup>13</sup> The final listing of the table presents the corresponding ideal performance assuming no manufacturing errors. These results demonstrate monotonic worsening of performance from the ideal case as the feature size is increased. In Figure 3, we show the output corresponding to a feature size of 0.1  $\mu\text{m}$  at both the pupil plane (P2) in Figure 3(a) and at the image plane (P3) in Figure 3(b). We present azimuthally averaged cross-sections as the feature size is increased for both suppression and contrast in Figures 3(c) and 3(d) respectively.

The most computationally expensive part of this numerical validation process for different feature sizes is the creation of the mask models. Since the suppression and contrast performance worsens monotonically with increasing feature sizes, we can compute estimates of the performance at intermediate feature sizes by applying a piecewise spline interpolation between the computed suppression and contrast results.

We can use these interpolated results to obtain an estimate of the performance of the occulter experiment as the total propagation distance is modified resulting in size changes of the occulter mask while manufacturing feature size is fixed. The relative size of the fixed feature sizes decreases as the total propagation distance and corresponding occulter mask radius increases, and, conversely the relative size increases as the mask shrinks when a smaller propagation distance is available. This process is applied for the suppression performance in Figure 4. In Figure 4(a), the computed mean suppression results across the telescope aperture are denoted by open circles corresponding to the mask models listed in Table 3. The mask models give us the computed feature sizes and we apply an interpolation to obtain the suppression curve at intermediate feature sizes. Based on the suppression curve as a function of feature size, we estimate the effect of changing the total propagation distance in Figure 4(b) while maintaining a fixed manufacturing feature size.

For aggressive 0.2  $\mu\text{m}$  and 0.5  $\mu\text{m}$  feature sizes, the suppression performance is better than  $10^{-9}$  for all testbed sizes greater than 65 m. For the 0.2  $\mu\text{m}$  feature size the considered testbed size of 76 m corresponds to a suppression performance of  $10^{-9.7}$  which is only a factor of 1.3 short off the ideal suppression.

For all the propagation distances and manufacturing feature accuracies greater than 0.5  $\mu\text{m}$  considered, the suppression performance is limited by the feature accuracy at more than half an order of magnitude from the ideal case. In Figure 5, we therefore consider large-scale sizing of the occulter similar for longer-distance field tests. The radial size of the occulter scaled at km separations is shown in Figure 5(a). The scaled suppression performance at these separations is shown for high-resolution feature sizes in Figure 5(b), and indeed the expected performance (if manufacturing feature sizes can be kept constant) approaches the ideal case. If 0.5  $\mu\text{m}$  can be maintained over a  $\approx 100$  mm mask diameter,  $\approx 2.5$  km scaling would be sufficient to achieve near ideal performance. However, it will be necessary to enclose the experiment in a tube that similarly scales in size, with a minimum diameter

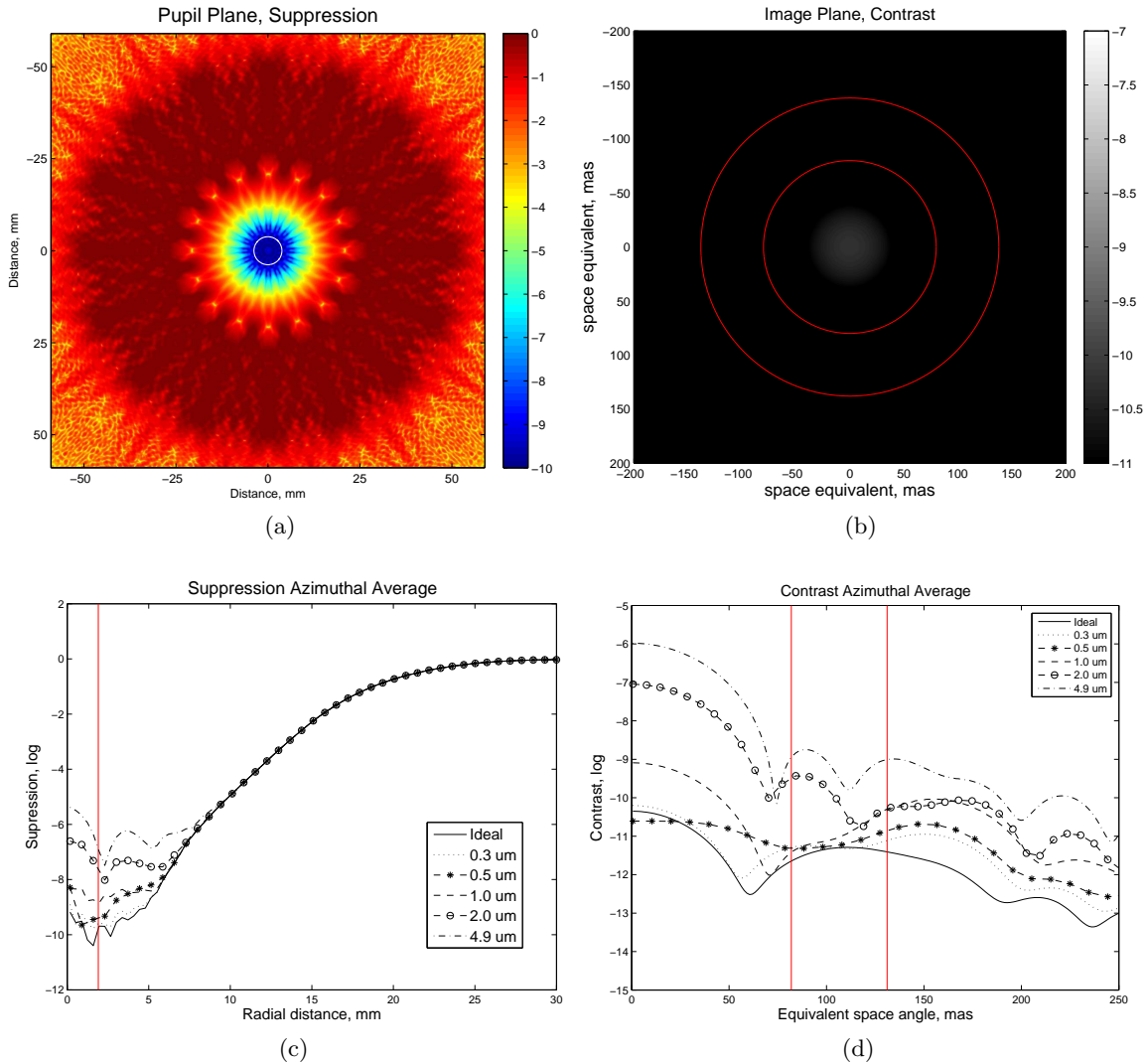


Figure 3: Model simulation results scaled for total propagation distance of 100 m and sensitivity for increasing feature sizes. Sample output for highest-accuracy model with feature size of 0.1  $\mu\text{m}$  featuring near-ideal performance: (a) Suppression at the laboratory pupil plane, and (b) contrast at the laboratory image plane. Comparison for increasing feature sizes: (c) Azimuthally averaged suppression across pupil plane with solid red line indicating extent of telescope aperture across which mean suppression is reported. Red line indicates extent of telescope aperture. (d) Azimuthally averaged contrast across image plane. Annular working zone is indicated by solid red line with inner working angle defined by inner occulter's petal tips and the outer working angle the outer ring's inner tips.

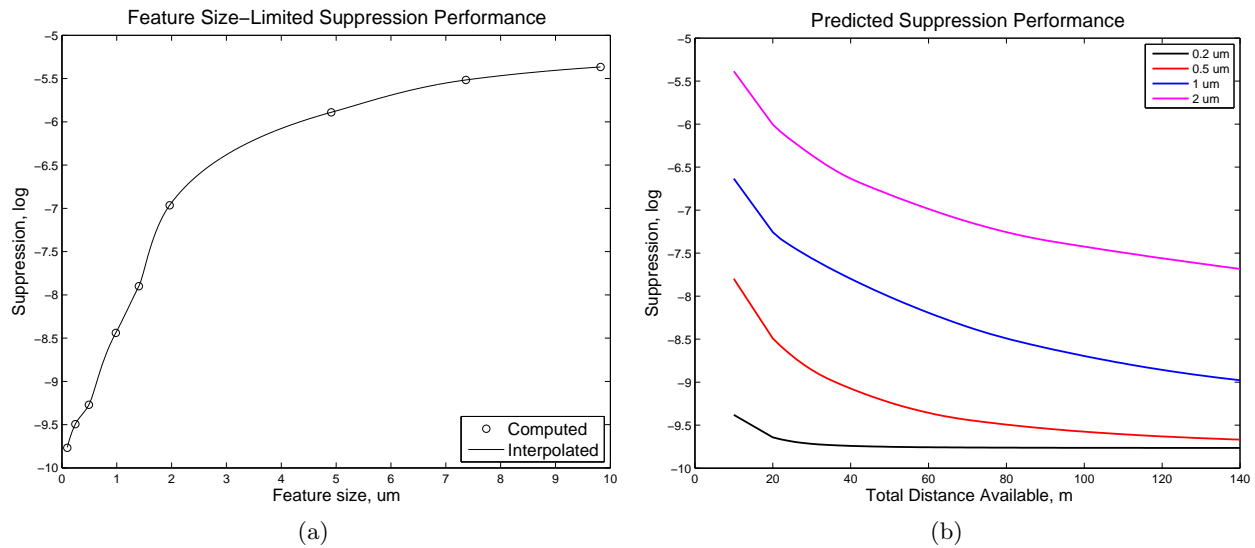


Figure 4: Suppression performance from computed manufacturing feature accuracy: (a) Computed suppression at different manufacturing feature size and interpolation for other feature sizes (b) Predicted suppression performance as a function of total propagation distance available for fixed manufacturing feature sizes. Dashed lines indicate 76 m and 100 m propagation distances which match the selected testbed size and the simulation reference respectively.

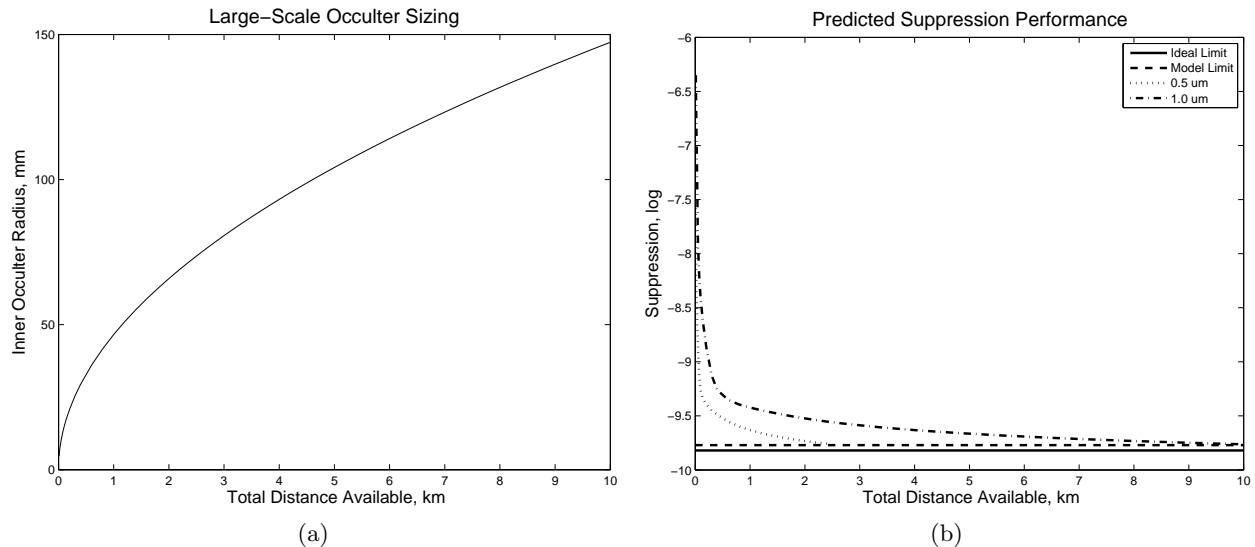


Figure 5: Large-scale occulter sizing and suppression performance (a) Radius of inner occulter sized under same diverging beam scaling with large-scale distance available (b) Expected suppression performance for large-scale occulter and comparison to ideal and model limits.

of 0.7 m at the 100 m propagation distance baseline scaling up to 5 m at 2.5 km. Details of the computation of tunnel diffraction effects are discussed in a dissertation<sup>11</sup> and a future publication.

These deterministic models are symmetrical, except for quantization errors arising from translation of a sixteen-fold circularly symmetric pattern to a rectangular grid, and therefore represent an optimistic bound on performance. We now consider the effect on performance due to the loss of symmetry that arises from perturbations at the mask edges that model manufacturing defects, that is differences from the prescribed mask edges. For example, consider the degradation in suppression and contrast performance in Figure 6(a) and Figure 6(b) respectively due to introduction of 2  $\mu\text{m}$  RMS edge errors. Performance with such stochastic manufacturing defects added represents a more conservative bound on performance. In Figure 6, we show the newly computed conservative, stochastic performance bound. Due to the stochastic nature, we perform ten trials for each considered edge defect diameter and report the mean suppression across the dark hole in Figure 6(c) and the mean contrast in Figure 6(d) across the annular working region. The piecewise spline interpolation is shown for intermediate defect sizes. In Figure 6(d), we plot the previously shown suppression performance curves in Figure 4 (b) corresponding to fixed feature sizes as the scaling of the mask is changed as a function of the total propagation distance available. In dashed lines we show the performance degradation due to the introduction of edge defects with the corresponding specified RMS levels.

When edge perturbations are considered, the suppression performance degrades. For example, at 0.2  $\mu\text{m}$  the suppression which was  $10^{-9.7}$  for the non-perturbed case is now  $10^{-9.5}$ . This is a factor of 2 short off the ideal. For a testbed of 76 m propagation distance, the 0.5  $\mu\text{m}$  is still expected to be better than  $10^{-9}$ . Therefore, as long as feature accuracy and edge deviations can be maintained at the desired 0.5  $\mu\text{m}$  level or better, a very deep suppression level can be verified.

We have thus shown through simulation that the PPOE will result in better expected performance than is possible for the EPOE. This is possible through two separate effects. First, increasing the propagation distance for the PPOE to 76 m from the existing 10 m while maintaining the same level of manufacturing errors over a mask design etched in the silicon wafer results in better suppression performance for an identical mask design scaled at these different distance. Second, improvements in manufacturing of occulter masks on silicon will reduce the errors on the manufactured occulter edge.<sup>13</sup>

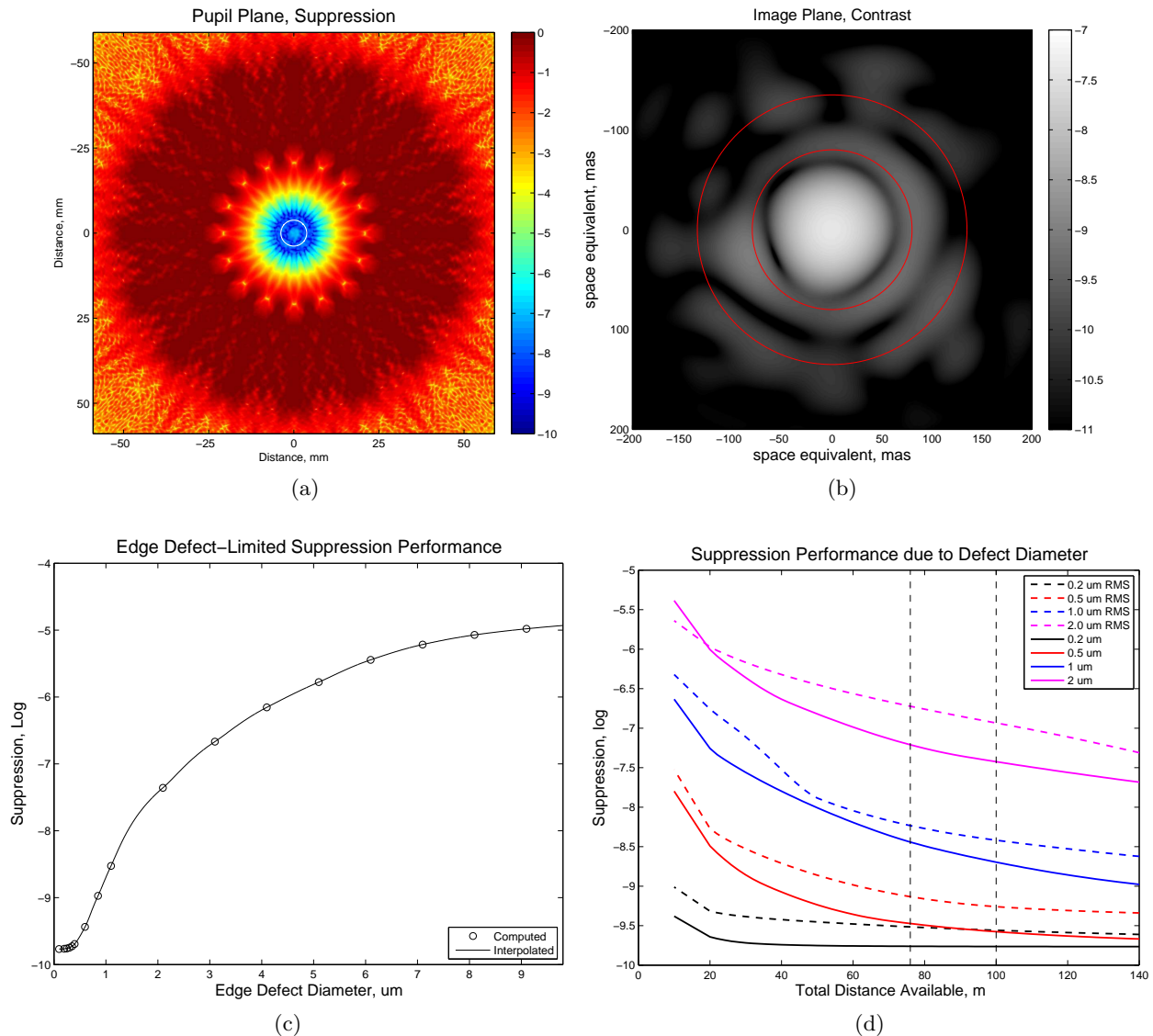


Figure 6: Performance of mask with white noise perturbations injected at the petal edges. Injected perturbations correspond to certain specified defect diameter RMS. Sample output showing performance degradation due to 2  $\mu\text{m}$  RMS edge defects: (a) Suppression at the laboratory pupil plane, and (b) contrast at the laboratory image plane (c) average suppression level from 10 trials corresponding to increasing edge defect diameter RMS and interpolation for intermediate defect diameters. (d) Suppression curves for different fixed feature sizes (solid lines) and edge defect diameter RMS (dashed lines) for varying total propagation distance available.

## 5. ANALYTICAL MODEL

We have developed a simple analytical model to corroborate the general behavior of the more complex numerical model. The model computes the ratio of the scatter at the pupil plane from a defect with dimension  $d$  in the mask plane to the light level at the pupil plane if the mask were not present. It then adds up the contributions of many such defects distributed along the edges of the mask, ignoring the coherent interference terms because we are only interested in the average suppression at the pupil plane.

The model is laid out in Figure 7. A point source in plane P0 illuminates the mask plane P1 distance  $h$  away with an irradiance of  $P$  W/m<sup>2</sup>. At the pupil plane P2, a distance  $z$  further downstream, the irradiance is reduced by the ratio of areas to  $P(h/(h+z))^2$  W/m<sup>2</sup>. Here, we have assumed that  $h$  and  $z$  are much larger than the transverse dimensions of the mask and pupil planes. A defect in P1, e.g., a hole or extra material near the edge of the mask, transmits or blocks the light, scattering power  $Pd^2$  through the plane. For defects larger than the wavelength, the light diverges over a solid angle of  $(\lambda/d)^2$  sr. The irradiance at plane P2 is then  $Pd^2/(z\lambda/d)^2$  W/m<sup>2</sup>. Finally, if the integrated length of the mask edge is  $L$ , then there are  $N = L/d$  potential defects along the edge. The ratio of the pupil plane energy received from the defects to the energy received from the point source is the suppression limit, given by:

$$R = \frac{Ld^3(h+z)^2}{(\lambda hz)^L a^2}, \quad d \gg \lambda. \quad (1)$$

For the mask located midway between the point source and the pupil plane,  $h = z$  and the expression simplifies to:

$$R = \frac{4Ld^3}{(\lambda h)^2}, \quad d \gg \lambda. \quad (2)$$

When the defects are sub-wavelength,  $d \ll \lambda$ , the divergence angle is independent of diameter and light is scattered over a solid angle of  $\lambda$  sr. In this case, the suppression limit is given by

$$R = \frac{Ld(h+z)^2}{\pi(hz)^2}, \quad d \ll \lambda. \quad (3)$$

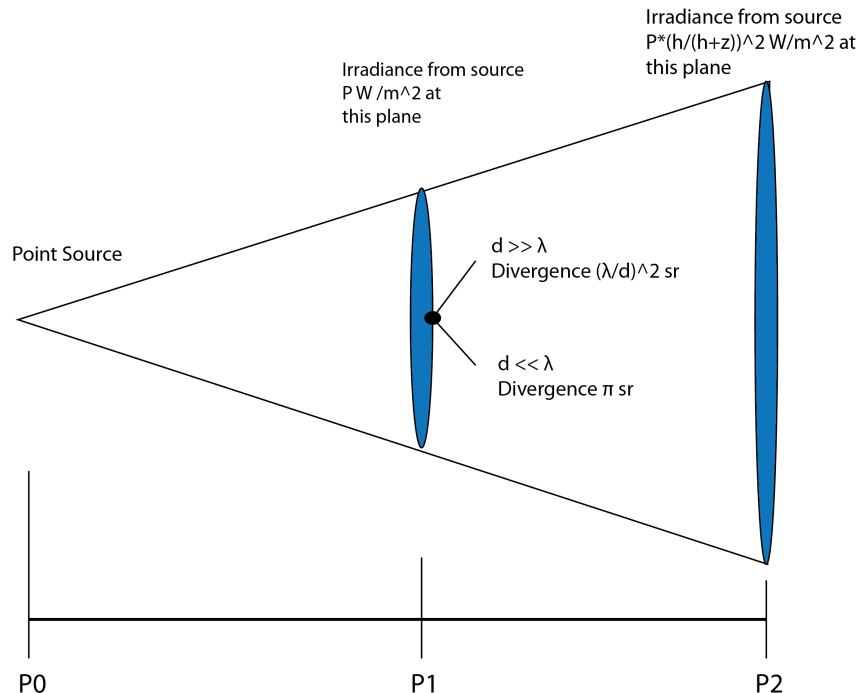


Figure 7: Schematic of analytical model for mask-defect scattering analysis.

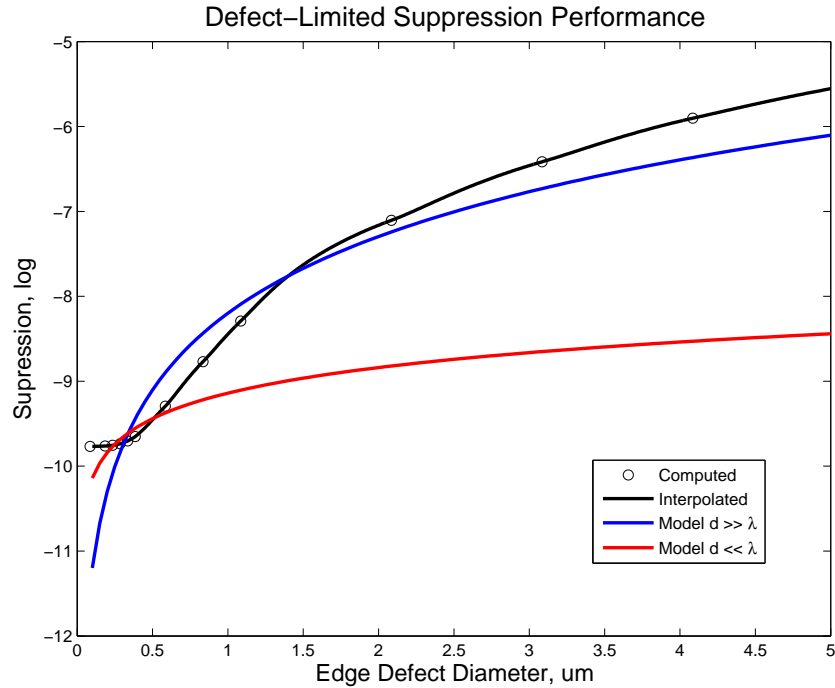


Figure 8: Comparison of simulated defect-limited suppression performance with analytical model for the PPOE scaled at 76 m propagation testbed for input light with  $\lambda = 633$  nm.

which reduces to

$$R = \frac{4Ld}{\pi h^2} \quad (4)$$

when the mask is midway between P0 and P2.

In Figure 8, we have plotted the result of the numerical simulation including the edge-perturbation modeling the effect of circular edge defects. We also plot the expected suppression curves corresponding to the analytical model for both defects smaller and greater than the wavelength  $\lambda$ . The curve of the numerical simulation flattens around 600 nm which is the simulated wavelength as predicted by the analytical model; we observe a transition region around 1  $\mu\text{m}$  where the numerical result is between the two model curves. For very small defect sizes, suppression approaches the actual diffraction-limit of the occulter design (not modeled for the analytical curve).

## 6. CONCLUSIONS

In this paper, we have used the optical model previously introduced and verified on the propagation distance-limited EPOE testbed<sup>4</sup> to determine the expected performance for an occulter mask scaled for the longer propagation-distance PPOE testbed featuring the same type of edge errors that have limited the performance of the current experiment. This numerical simulation has been used to show the sensitivity to total propagation distance available and it was shown that the PPOE scaled at 76 m and with mask designs specified at sub- $\mu\text{m}$  will achieve a suppression level better than  $10^{-8}$ . For an improved manufacturing process with 0.2 – 0.5  $\mu\text{m}$  features the achievable suppression performance is better than  $10^{-9}$ . These correspond to contrast levels better than  $10^{-10}$  consistent with the level required for an occulter mission capable of imaging exo-Earths.

We have also developed an analytical model to predict the suppression limitation due to edge defects at the occulter edges and compared this model with the numerical simulations. The analytical model can be used to examine trends and predict scaled performance of an occulter mask for different manufacturing accuracies without requiring a more complicated numerical simulation.

In this investigation we have rescaled the PPOE baseline occulter mask design to study the effect of the total available distance for the propagation testbed and to choose a location for the expanded testbed. For very small manufacturing defects, additional performance improvements can be achieved from mask designs optimized to suppression levels deeper than the baseline PPOE mask we used in this paper can be achieved. The latest occulter mask designs for the PPOE thus feature improved performance in part by optimizing the occulter mask to minimize the perimeter of the occulter mask.<sup>14</sup>

## ACKNOWLEDGMENTS

This work was partially performed under NASA contract NNX09AB97G and grant 1430187 from the California Institute of Technology's Jet Propulsion Laboratory. DS acknowledges financial support from the NASA Earth & Space Science Fellowship and the NASA Postdoctoral Program.

## REFERENCES

1. N. J. Kasdin *et al.*, "A Telescope for Habitable Exoplanets and Interstellar/Intergalactic Astronomy," *White Paper*, 2009. [http://exep.jpl.nasa.gov/stdt/Exo-S\\_Starshade\\_Probe\\_Class\\_Final\\_Report\\_15031\2\\_URS250118.pdf](http://exep.jpl.nasa.gov/stdt/Exo-S_Starshade_Probe_Class_Final_Report_15031\2_URS250118.pdf).
2. S. Seager *et al.*, "Exo-S: Starshade probe-class exoplanet direct imaging mission concept," *White Paper*, 2015. [http://exep.jpl.nasa.gov/stdt/Exo-S\\_Starshade\\_Probe\\_Class\\_Final\\_Report\\_15031\2\\_URS250118.pdf](http://exep.jpl.nasa.gov/stdt/Exo-S_Starshade_Probe_Class_Final_Report_15031\2_URS250118.pdf).
3. N. J. Kasdin *et al.*, "Recent progress on external occulter technology for imaging exosolar planets," *Proceedings of the IEEE Aerospace Conference*, 2013.
4. D. Sirbu, N. J. Kasdin, and R. J. Vanderbei, "Diffractive analysis of limits of an occulter experiment," *Proc. SPIE* **9143**, 2014.
5. R. J. Vanderbei, E. J. Cady, and N. J. Kasdin, "Optimal occulter design for finding extrasolar planets.," *Astrophysical Journal* **665**, pp. 794–798, 2007.
6. R. J. Vanderbei, D. N. Spergel, and N. J. Kasdin, "Circularly symmetric apodization via star-shaped masks.," *Astrophysical Journal* **599**, pp. 686–694, 2003.
7. E. Cady *et al.*, "Progress on the occulter experiment at Princeton," *Proc. of SPIE*, 2009.
8. E. Cady, *Design, Tolerancing, and Experimental Verification of Occulters for Finding Extrasolar Planets*. PhD thesis, Princeton University, 2010.
9. D. Sirbu, N. J. Kasdin, and R. J. Vanderbei, "Monochromatic verification of high-contrast imaging with an occulter," *Optics Express* **21**, 2013.
10. N. J. Kasdin *et al.*, "O3: The Occulting Ozone Observatory," *Bulletin of the American Astronomical Society*, 2010.
11. D. Sirbu, *Occulter-Based High-Contrast Exoplanet Imaging: Design, Scaling, and Performance Verification*. PhD thesis, Princeton University, 2014.
12. R. Soummer, L. Pueyo, A. Sivaramakrishnan, and R. J. Vanderbei, "Fast computation of Lyot-style coronagraph propagation," *Optics Express* **15**.
13. K. Balasubramanian *et al.*, "Fabrication and characterization of exoplanet coronagraph shaped pupil masks and laboratory scale star-shade masks," *Proc. SPIE* **9605**, 2015.
14. Y. Kim, M. Galvin, N. J. Kasdin, R. J. Vanderbei, D. Ryu, and D. Sirbu, "Design of a laboratory testbed for external occulters at flight Fresnel numbers," *Proc. SPIE* **9605**, 2015.